Monthly Notices
of the
ROYAL ASTRONOMICAL SOCIETY

MNRAS **435,** 845–860 (2013)
Advance Access publication 2013 August 19

doi:10.1093/mnras/stt1354

The numbers of $z \sim 2$ star-forming and passive galaxies in 2.5 square degrees of deep CFHT imaging

Liz Arcila-Osejo★ and Marcin Sawicki

Department of Astronomy & Physics and the Institute for Computational Astrophysics, Saint Mary's University, 923 Robie Street, Halifax, Nova Scotia B3H 3C3, Canada

Accepted 2013 July 19. Received 2013 July 19; in original form 2013 March 6

ABSTRACT

We use an adaptation of the BzK_s technique to select ∼40 000 $z \sim 2$ galaxies (to $K_{AB} = 24$), including ∼5000 passively evolving (PE) objects (to $K_{AB} = 23$), from 2.5 deg^2 of deep Canada–France–Hawaii Telescope (CFHT) imaging. The passive galaxy luminosity function (LF) exhibits a clear peak at $R = 22$ and a declining faint-end slope ($\alpha = -0.12^{+0.16}_{-0.14}$), while that of star-forming galaxies is characterized by a steep faint-end slope [$\alpha = -1.43 \pm 0.02(\text{systematic})^{+0.05}_{-0.04}(\text{random})$]. The details of the LFs are somewhat sensitive (at the <25 per cent level) to cosmic variance even in these large (∼0.5 deg^2) fields, with the D2 field (located in the Cosmological Evolution Survey, COSMOS field) most discrepant from the mean. The shape of the $z \sim 2$ stellar mass function of passive galaxies is remarkably similar to that at $z \sim 0.9$, save for a factor of ∼4 lower number density. This similarity suggests that the same mechanism may be responsible for the formation of passive galaxies seen at both these epochs. This same formation mechanism may also operate down to $z \sim 0$ if the local PE galaxy mass function, known to be two-component, contains two distinct galaxy populations. This scenario is qualitatively in agreement with recent phenomenological mass-quenching models and extends them to span more than three quarters of the history of the Universe.

Key words: galaxies: evolution – galaxies: formation – galaxies: luminosity function, mass function.

1 INTRODUCTION

One of the main challenges in observational cosmology is trying to understand the formation and evolution of galaxies based on their dark and baryonic components, specifically to test theoretical models of galaxy formation at every redshift. A large number of surveys have been developed during the last decade to construct multiwavelength observations of galaxies using diverse ground- and space-based facilities. These surveys strive to understand how the galaxy populations observed at early times evolved into those in our local Universe. An important feature to be able to model is how the most massive galaxies seen locally have assembled most of their mass and what type of evolution characterized this growth. A critical epoch for galaxy formation was $2 \leq z \leq 4$, when star formation activity in the Universe was at its peak, and most of the structures that we observe in the local Universe were not yet present (Shapley 2011). However, a specific evolutionary path from this redshift to the present time is still undetermined (McCracken et al. 2010; Shapley 2011).

Building large statistical samples of galaxies allows us to explore galaxy populations at early epochs and to develop a more complete view of the evolution of structure in our Universe. Large infrared (IR)-selected samples are essential for many reasons: (1) spectral features at these important redshifts move out of the optical into the near-IR, (2) long wavelengths are less affected by dust attenuation and – especially – (3) observations at these wavelengths more closely correspond to stellar mass-selected samples since the flux comes from low-mass, cooler stars that represent most of the mass of the system.

A complete exploration of galaxies at these epochs would require large spectroscopic IR surveys, which are time consuming and realistically unfeasible. Colour–colour selection techniques serve as an efficient way of constructing large samples of galaxies. These selection methods have been developed to distinguish between star-forming (SF) and passive galaxies. This distinction can be used to infer information that can be useful for understanding the evolution of the two populations.

Some examples of such colour–colour criteria used to select high-redshift galaxies are the Lyman break galaxies (Steidel et al. 1999, 2003), BX and BM galaxies (Steidel et al. 2004), extremely red objects (EROs; Elston et al. 1988; Thompson et al. 1999; Roche et al. 2002; Messias et al. 2010), distant red galaxies (DRGs; Franx et al. 2003) and BzK_s selection (Daddi et al. 2004a). The Lyman break and BX/BM techniques were developed to select $z \sim 2$–3 SF galaxies, but miss many passively evolving (PE) and/or heavily dust-reddened objects. The ERO and DRG techniques are designed to select

★ E-mail: liz.arci3@gmail.com

passive high-redshift galaxies based on their red colours. However, a spectroscopic follow-up shows that these samples include both passive galaxies and dust-reddened SF galaxies (Cimatti et al. 2002; van Dokkum et al. 2004). Of all of these techniques, the BzK_s selection technique is the only one able to select and distinguish between SF and passive galaxies at $z \sim 2$ (Daddi et al. 2004a; Grazian et al. 2007). This ability provides a way to trace the evolution of these different populations to high redshift, thereby providing a more complete picture of galaxy formation and evolution. Consequently, the BzK_s technique has enjoyed much popularity in recent years (e.g., Kong et al. 2006; Lane et al. 2007; McCracken et al. 2010; Bielby et al. 2012). However, despite this prominence even such a basic property of the BzK_s population as its luminosity function (LF) is still only poorly constrained, and especially so for passive BzK_s galaxies.

In this work, we adapt the BzK_s selection criteria to the filter set used in the optical and IR observations of the Canada–France–Hawaii Telescope Legacy Survey (CFHTLS). We apply our selection criteria to these large fields (0.4–0.9 deg^2 each) and independent lines of sight in the four Deep Fields of the CTHTLS to construct large, statistically representative samples of SF and passive galaxies at $z \sim 2$. We then constrain the number counts, rest-frame R-band LFs and stellar mass functions (SMFs) of both the SF and passive populations. The four separate lines of sight and large effective areas provide low statistical uncertainties while at the same time monitoring the field-to-field fluctuations due to cosmic variance.

Throughout this work we use a flat lambda cosmology ($\Omega_{\rm m} = 0.3$, $\Omega_\Lambda = 0.7$) with $H_0 = 70\,{\rm km\,s^{-1}\,Mpc^{-1}}$. Unless stated otherwise, we use the AB magnitude system (Oke 1974) and the Salpeter (1955) stellar initial mass function (IMF) throughout.

2 DATA

Our data consist of a combination of two deep wide-field public data sets, one optical and one IR, taken primarily with the 3.6 m Canada–France–Hawaii Telescope (CFHT) on Mauna Kea. The optical data are the four Deep Fields of the CFHTLS (The CFHTLS T0006 Release; Goranova et al. 2009); the IR data are from the deep imaging in these CFHTLS fields done by the WIRCam Deep Survey (WIRDS; Bielby et al. 2012). Together, these four fields, referred to as D1, D2, D2 and D4, cover a total area of 2.47 deg^2 and have significant overlap with regions of the sky that have been extensively studied in other surveys, including the Cosmological Evolution Survey (COSMOS) (D2) and the Groth Strip (D3); see, e.g., Gwyn (2012) and references therein. Each of the four fields is large and widely separated on the sky to sample variance (cosmic variance). This can be expected to be a significant contributor to any observed differences between the fields.

Although we are aware of the existence of other data sets, such as UltraVISTA and the VISTA Deep Extragalactic Observations (VIDEO), which may provide better coverage of some fields or better depths, these data sets were not available at the time this paper was being developed so we have not included them in our analysis.

2.1 Optical data: the CFHTLS Deep Fields

The CFHTLS is a large project carried out by Canada and France that used 50 per cent of the dark and grey telescope time from mid-2003 to early 2009. For the present work, we used the Deep Survey component of the CFHTLS, which was originally developed to detect 500 Type Ia supernovae and to study the galaxy distribution down to a limiting magnitude $r' = 28$.

The CFHTLS was carried out using MegaCam which is the wide-field optical imager at MegaPrime, the wide-field facility at CFHT. MegaCam has thirty-six 2048 × 4612 pixel CCDs covering a 1 deg × 1 deg field of view with a total of 340 megapixels with a resolution of 0.186 arcsec pixel^{-1}. The CFHTLS Deep Survey consists of four widely separated 1 deg^2 fields – labelled D1, D2, D3, D4 – each of which was observed in five broad-band filters (u^*, g', r', i', z'). Each one of these bands with an 80 per cent completeness (stellar/compact objects) of 26.22 ± 0.10, 25.94 ± 0.10, 25.40 ± 0.10, 25.10 ± 0.10 and 25.59 ± 0.10, respectively.[1] These filters were designed to match the Sloan Digital Sky Survey (SDSS) filters as closely as possible except for the u^* filter, which is designed to take advantage of Mauna Kea's lower UV extinction than that at the Apache Point site of the SDSS.

We used the CFHTLS T0006 data release which contained two sets of images, one with the 85 per cent best seeing images and the other with the 25 per cent best seeing images. While the 85 per cent image stacks are deeper than the 25 per cent stacks for extended sources, our tests showed that the difference was small for compact galaxies such as our high-redshift objects. Consequently, we chose to use the 25 per cent images as these also give us the potential to better investigate morphologies or close companions in future work.

Several entities were involved in the acquisition and processing of CFHTLS data: CFHT was used for data acquisition and calibration while the pre-processing of the images was done by TERAPIX.[2] Pre-processing involves image quality checking, flat fielding, stacking from dithered images, identification of bad pixels, removal of cosmic rays and saturated pixels, background estimation and subtraction, and astrometric and photometric calibration.

2.2 IR data: WIRDS

WIRDS is a large project that obtained deep J, H and K_s imaging of large subareas of the four CFHTLS Deep Fields. WIRDS was carried out between 2006 and 2008, with the bulk of the data being obtained at CFHT using WIRCam (Marmo 2007), but one image (the J-band image of the D2 field) was obtained using the Wide Field Camera (WFCAM) instrument on the United Kingdom Infrared Telescope (UKIRT).

WIRCam has four detectors in a 2 × 2 array with 2048 × 2048 active pixels and covers a 20 arcmin × 20 arcmin field of view with a sampling of 0.3 arcsec pixel^{-1}. The WIRCam images have been re-sampled to match the 0.186 arcsec pixel^{-1} MegaCam pixel scale.

Pre-processing of the WIRDS data includes a reduction process as follows: bias subtraction and flat-fielding, initial sky subtraction, cross-talk correction, second-pass sky subtraction, astrometric and photometric calibration and the production of final processed image stacks. For this project, we used the WIRDS T0002 data release. For the details of the WIRDS data processing, see Bielby et al. (2012).

2.3 Object detection and photometry

We used SExtractor version 2.8.6 (Source Extractor; Bertin & Arnouts 1996) for object detection and photometry. Object detection was done in the unsmoothed K_s images. SExtractor parameters

[1] Strictly speaking, the CFHTLS i'-band observations used two slightly different i' filters, but since we do not use i'-band data in this work, we do not discuss this issue further.

[2] Traitement Élémentaire Réduction et Analyse des PIXels, Institut d'Astrophysique de Paris, http://terapix.iap.fr

Table 1. Summary of our four fields. Effective areas are given in deg^2 after removing masked regions. Also shown is the colour excess $E(B-V)$ at the centre of each field and the number of objects found to $K_s = 23.0$. When a range is given, the lower number indicates the number of galaxies that are unambiguously at $z \sim 2$, while the higher number includes those objects that cannot be ruled out as low-z interlopers.

Field	Effective area (deg^2)	$E(B-V)$	All objects	*gzHK*	PE-*gzHK*	SF-*gzHK*
D1	0.68	0.0254	55 256	11 258–12 281	1382	9972–11 004
D2	0.89	0.0162	87 206	12 238–15 222	1739	10 880–13 835
D3	0.45	0.0072	37 380	7046–7668	841	6223–6845
D4	0.45	0.0275	38 461	7312–8168	1013	6361–7226

were tuned to detect the vast majority of objects identifiable by eye without producing significant numbers of spurious detections; in practice, this meant that we required that an object should have a minimum of five contiguous pixels above the 1.2σ sky level in the WIRDS K_s image. Kron-like apertures (Kron 1980), in which the first image moment is used to determine the flux of the galaxy from a circular/elliptical aperture (Graham et al. 2005), were used to determine the total magnitude of a galaxy.

To ensure accurate colours, object colours were measured on point spread function (PSF) matched images through matched apertures. The PSF matching involved local PSF determination within the images, followed by smoothing to match the local PSF in the worst seeing image in each field. It takes into account seeing variations across the large, multichip mosaics used here. For full details of the PSF matching, see the paper by Sato, Sawicki & Arcila-Osejo (in preparation). Fluxes within 1.86 arcsec (10 pixel)-diameter apertures were then determined at the positions of the K_s-band detections using SExtractor's dual-image mode, and these fluxes were then combined to produce object colours.

Corrections for extinction due to dust in our Galaxy were made based on the Schlegel, Finkbeiner & Davis (1998) dust maps, using the $E(B-V)$ value at the centre of each field (see Table 1) to correct the magnitudes and colours of all the objects in that field. Because extinction is small in the CFHTLS Deep Fields, dust corrections are likewise small and using the central field values is a reasonable approximation.

Next, we masked out suspect areas of the images from our final science catalogue. These areas consist of regions likely to yield spurious detections or suspect photometry and include areas near stellar diffraction spikes, bleeding columns, residual satellite trails or reflective haloes from bright stars caused by reflections from the CCD and instrument optics. Unexposed areas (based on weight images supplied by TERAPIX) are also excluded. Additionally, using SExtractor's internal flags, we are able to identify saturated and/or truncated objects in our sample. Rejecting these objects flagged by SExtractor does not represent a considerable loss of data (approximately only 1.6 per cent of our sample), but ensures the removal of objects whose colours may be inaccurate.

Table 1 gives a summary of the four Deep Fields, the resulting effective area after the masking of suspect regions, the colour excess at the field centre and the number of objects found in each field to $K_s = 23.0$.

3 THE *gzHK*$_s$ SELECTION AND CLASSIFICATION OF $z \sim 2$ GALAXIES

Daddi et al. (2004a) developed the BzK_s selection technique to select $z \sim 2$ galaxies and classify them into SF and PE objects. The CFHTLS+WIRDS g', z' and K_s filters differ from the Daddi et al. filters and so it is necessary to adjust our approach to account for that. While some studies transform the colours of their observed objects to bring them on to the BzK_s system (e.g. Kong et al. 2006; Blanc et al. 2008; Hartley et al. 2008; McCracken et al. 2010), we use a different approach in that we work in the native $g'z'K_s$ filter set of our data and instead adapt the colour selection cuts to match this filter set, as described in Section 3.1.

One strength of the BzK_s technique is its ability to distinguish between $z \sim 2$ SF and passive galaxies. However, because a typical PE galaxy at $z \sim 2$ is expected to have very red colours (typically $B - K > 5$), this approach requires extremely deep observations at blue wavelengths. Since we wish to probe as deep into the $z \sim 2$ LFs as our K_s-band selection allows ($K_s \lesssim 23$–24), and since our optical data are not particularly deep in comparison, in Section 3.3 we develop a modification to the gzK_s technique that, by incorporating H-band photometry, allows us to reliably discriminate between SF and passive galaxies without the need for ultra-deep blue data. We thus follow a two-step process: gzK_s selection to select $z \sim 2$ galaxies without knowledge of their spectral type (Section 3.2) followed by zHK_s-based classification into SF and passive populations (Section 3.3).

A similar analysis was performed to ensure that our z band was deep enough to avoid low-redshift interlopers or mistakenly classify SF galaxies as passive. We found that contamination of the blue population by z-band non-detections is negligible, while that of the red population is only about 3 per cent.

To model galaxy colours, following the colour–colour criteria of Daddi et al. (2004a), we use rest-frame model spectra of constant star formation rate (SFR) and single-burst stellar populations from the GALAXEV library (Bruzual & Charlot 2003). Using solar metallicity models and the Salpeter (1955) stellar IMF, we apply attenuation by interstellar dust (Calzetti et al. 2000), redshifting to the observed frame and integration through the filter transmission curves using the SEDFIT package (Sawicki 2012a).

3.1 Galaxy models in the BzK_s and gzK_s diagrams

Daddi et al. (2004a) developed a highly popular technique that allows both the selection and classification of $z \sim 2$ galaxies using a simple BzK_s colour–colour diagram. Reproducing the BzK_s selection diagram of Daddi et al. (2004a), in the top-left panel of Fig. 1 we plot SF Bruzual & Charlot (2003) constant star formation (CSF) models with ages between 10^{-3} and 2 Gyr, solar metallicity, Salpeter stellar IMF, $0 \leq E(B-V) \leq 0.6$ and $1.4 \leq z \leq 2.5$. As shown in the bottom-left panel of Fig. 1, passive galaxies are represented using instantaneous burst models (single stellar population, SSP) with older stellar populations (ages between 0.1 and 2 Gyr), and no dust. In the BzK_s technique, high-redshift objects are uniquely located in regions of the BzK_s diagram: objects that lie to the left of the diagonal line are considered to be SF $z \sim 2$ galaxies, while those to the right of the diagonal line but above the

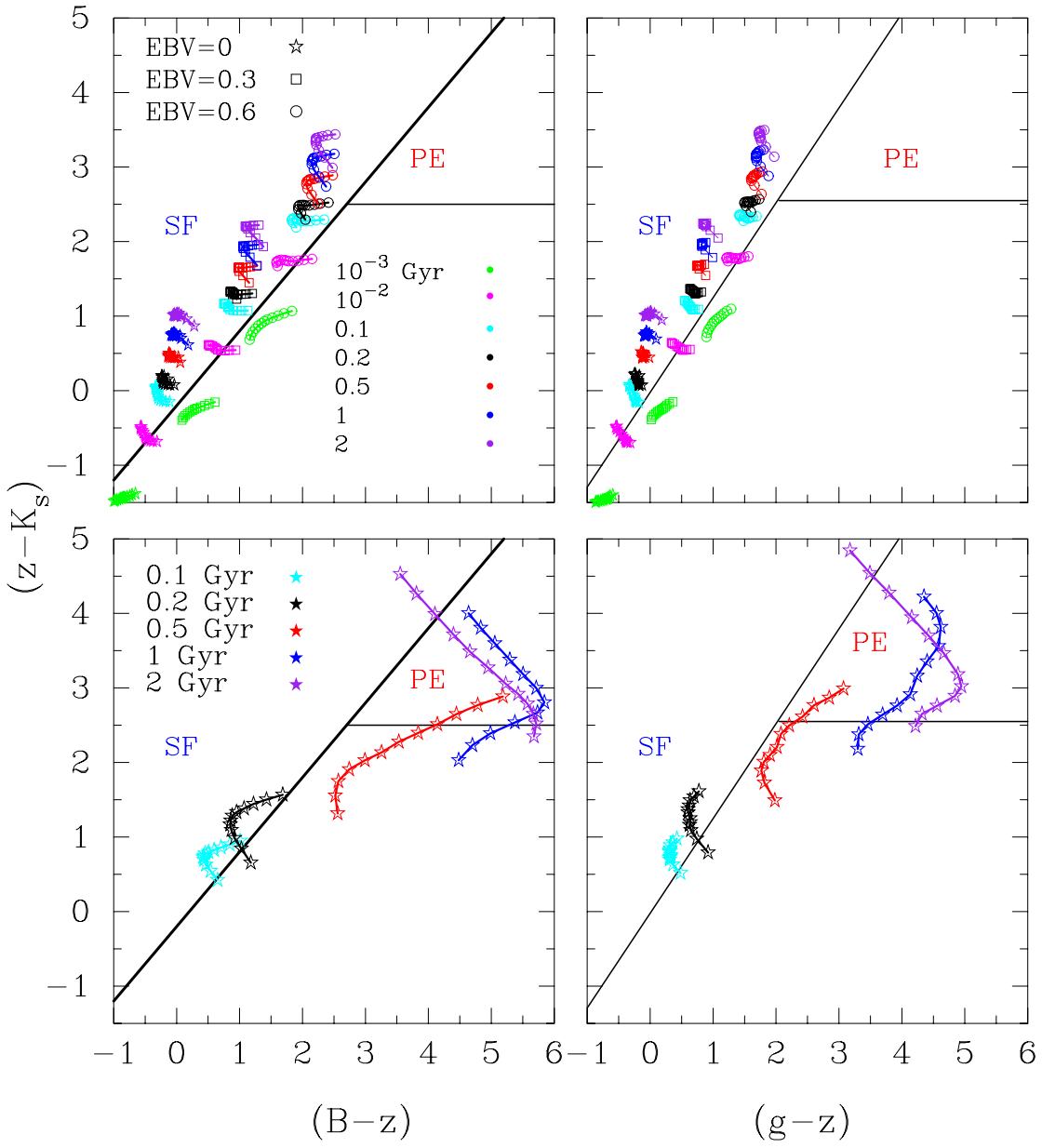

Figure 1. Bruzual & Charlot (2003) stellar population synthesis models for BzK_s and gzK_s colour–colour plots with $1.4 \leq z \leq 2.5$. Top-left panel: these models are intended to reproduce BzK_s colours of SF galaxies. Ages in Gyr are shown with different colours while different $E(B-V)$ are represented with different symbols. Top-right panel: the same CSF models shown previously in the BzK_s plot are simulated by the CFHT gzK_s filters. Bottom-left panel: instantaneous burst (SSP) models. These models are intended to reproduce BzK_s colours of passive galaxies with different ages and $E(B-V) = 0$. Bottom-right panel: the same SSP models shown in the bottom-left panel but in a gzK_s colour–colour plot. The solid black lines on the left-hand side of the plots are the same as given by Daddi et al. (2004a). The solid black lines in the right-hand side of the plots are shifted from the original criteria to select the same BzK_s models.

horizontal line are considered $z \sim 2$ PE galaxies. Spectroscopy, along with morphological studies, supports the validity of this approach (Daddi et al. 2004a,b; Ravindranath et al. 2008; Mancini et al. 2010; Onodera et al. 2010).

The location of galaxies in the colour–colour diagram (Fig. 1) may be affected by the choice of IMF, dust models or other model parameters. Such effects could affect the selection of high-z galaxies as well as their classification into passive and SF populations, and we plan to investigate the scope of these effects in future work; in the present paper, we simply use the models as described above since they provide consistency with the basic Daddi et al. (2004a) technique and the many papers that follow it.

To modify the BzK_s technique for use with the CFHTLS+WIRDS gzK_s filters, we considered the positions of the Daddi et al. (2004a) models (left-hand panels of Fig. 1) in the gzK_s colour–colour diagram (right-hand panels of Fig. 1). While the gzK_s and BzK_s filter systems are different, they are similar enough that the main qualitative features of the colour–colour diagram are preserved, as can be seen by comparing the left- and right-hand panels of Fig. 1. We conclude that even though the filters are somewhat different, we can adjust the original Daddi et al. (2004a) BzK_s selection to develop a gzK_s colour–colour selection.

In analogy with the BzK_s technique, we define lines in gzK_s colour–colour space that delineate regions inhabited by different

types of galaxies. These colour–colour cuts are defined by identifying the models that in the BzK_s space lie close to the Daddi et al. (2004a) BzK_s criteria, locating the corresponding models in the gzK_s colour–colour space, and then designing simple colour cuts in gzK_s space in analogy with those in the BzK_s diagram. Our adopted gzK_s colour cuts are shown with black lines in the right-hand panels of Fig. 1 and are described as follows. SF gzK_s galaxies can be selected using

$$(z - K_s) - 1.27(g - z) \geq -0.022, \quad (1)$$

and PE ones via

$$(z - K_s) - 1.27(g - z) < -0.022 \cap (z - K_s) > 2.55. \quad (2)$$

Finally, in analogy with the BzK_s technique, by visual inspection of the data we identify the stellar locus and distinguish between stars and galaxies using

$$(z - K_s) - 0.45(g - z) \leq -0.57. \quad (3)$$

It is important to note that our high-redshift selection criteria (equations 1 and 2) are designed in close reference to the BzK_s criteria of Daddi et al. (2004a) via the comparison of model locations in the two colour–colour spaces. Consequently, the galaxy populations selected by our new gzK_s criteria can be expected to closely match those selected using the traditional BzK_s technique.

3.2 Selection of $z \sim 2$ galaxies in the CFHTLS Deep Fields

In principle, our gzK_s selection criteria (equations 1 and 2) allow us to select and classify high-redshift galaxies in a way that closely resembles the popular BzK_s technique of Daddi et al. (2004a) but are directly applicable to the gzK_s CFHTLS+WIRDS filter set. However, as can be seen in Fig. 1, high-redshift galaxies are expected to have very red colours, so the use of gzK_s (or BzK_s) selection alone requires very deep g' (or B) data. With $K_{s,\rm lim} \sim 23$–24, we would require optical data reaching $g' \sim 28$–29 in order to discriminate between passive and SF $z \sim 2$ galaxies. The current CFHTLS data, as deep as they are for such a wide survey, are not deep enough.

This limitation is illustrated in Fig. 2. Although our data allow us to identify all objects with $z - K_s > 2.55$ as high redshift ($z \sim 2$), the majority of these galaxies are undetected in g' and so we cannot tell whether they are passive or SF $z \sim 2$ objects. We also face a lesser, but related problem in that a fraction of the galaxies with $z - K_s < 2.55$ is undetected in g', making it unclear whether they are $z \sim 2$ galaxies or low-redshift objects. One solution to these problems would be to obtain much deeper g' data than those already in hand, but this approach would be very costly in telescope time. Instead, we take a different approach, as follows.

While unable to usefully distinguish between SF and passive galaxies, the present data are deep enough to select $z \sim 2$ galaxies [albeit with redshift ambiguity for the relatively small number of g'-undetected objects below $(z - K_s) = 2.55$]. In other words, the union of the regions defined by equations (1) and (2),

$$(z - K_s) - 1.27(g - z) < -0.022 \cup (z - K_s) > 2.55, \quad (4)$$

selects all $z \sim 2$ galaxies so long as they are detected in g'.

We thus adopt equation (4) as our way to select *all* $z \sim 2$ galaxies. By either including or excluding the g' non-detections in our accounting, we then construct two conservative samples: one sample includes all objects that could be SF $z \sim 2$ galaxies (but with some lower-z contamination); the other consists only of objects that are sure to be $z \sim 2$ SF galaxies, but is not complete in the sense that it lacks those $z \sim 2$ star formers that are undetected in g'. The number of galaxies in these samples is listed in Table 1 under the heading '$gzHK_s$'.

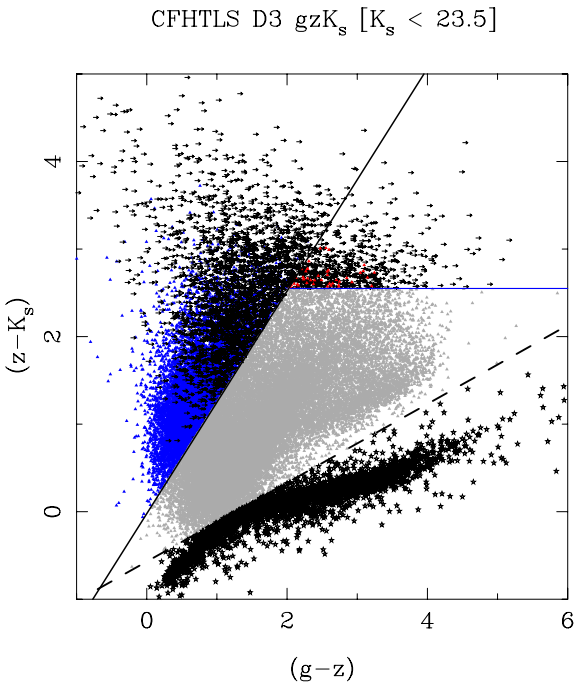

Figure 2. Objects in field D3 down to $K_s = 23.5$. Objects detected in g and classified as SF high-redshift galaxies are represented by blue triangles, while those detected in g and classified as passive galaxies are shown with red triangles. The arrows represent 1σ limits for objects that have not been detected in g. Stars reside in the lower right of the diagram and are shown with star symbols. The solid lines represent the colour cuts defined by equations (1) and (2), and the dashed line shows the stellar cut of equation (3).

The above approach does not give us information on the evolutionary states of our $z \sim 2$ galaxies. Consequently, to determine whether these galaxies are SF or passive, we develop a new technique, described in Section 3.3.

3.3 Classification into passive and SF populations using zHK_s colours

In Section 3.2, we defined samples of $z \sim 2$ galaxies in the CFHTLS Deep Fields. All $z \sim 2$ galaxies below $z - K_s = 2.55$ are by definition SF, but we were unable to determine the evolutionary state of the $z \sim 2$ galaxies above $z - K_s = 2.55$ using the gzK_s technique alone because we lack sufficiently deep g' data. To address the passive/SF ambiguity above $z - K_s = 2.55$, we now develop and apply a follow-up selection technique based on $(z - H)$ versus $(H - K_s)$ colours.

The red colour of $(z' - K_s) > 2.55$ galaxies is caused either by dust (in the case of SF objects) or by the presence of the 4000 Å/Balmer break complex (for sufficiently old passive systems). Dust attenuation of SF spectra produces a continuous, tilted spectral slope, while, in contrast, the 4000 Å/Balmer break complex gives a sharp spectral discontinuity. Consequently, it should be possible to distinguish between the two phenomena, and therefore between dusty star formers and passive systems, by adding a flux measurement between the z' and K_s bandpasses. Specifically, at $z \sim 2$, the 4000 Å/Balmer break complex is redshifted to ~11 000–12 000 Å and so will fall between

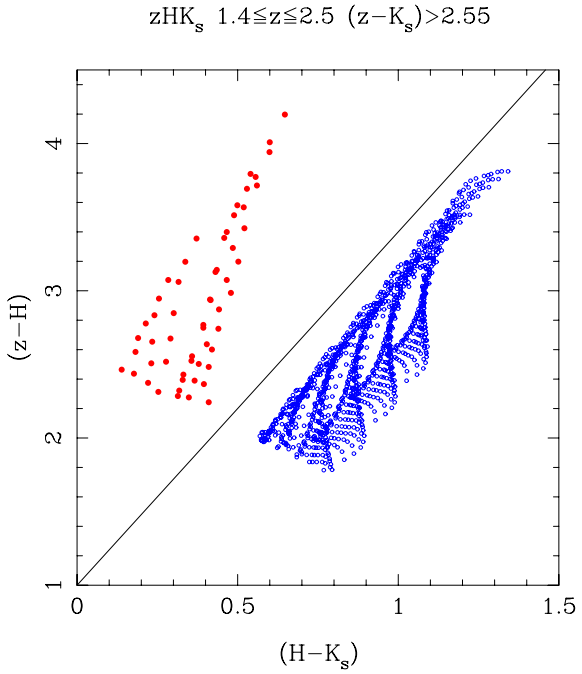

Figure 3. Model $(z - H)$ versus $(H - K_s)$ colours for those objects with $(z - K_s) > 2.55$ in the gzK_s diagram (see Fig. 1). The blue points represent SF galaxies with $\log_{10}$(Age) between 7.28 and 9.36 (0.02 and 2 Gyr) and $E(B - V) \geq 0$. The red points represent passive galaxies with $\log_{10}$(Age) between 8.63 and 9.36 (0.4 and 2 Gyr) and $E(B - V) = 0$. The solid line separates the SF and passive regions described by equations (5) and (6).

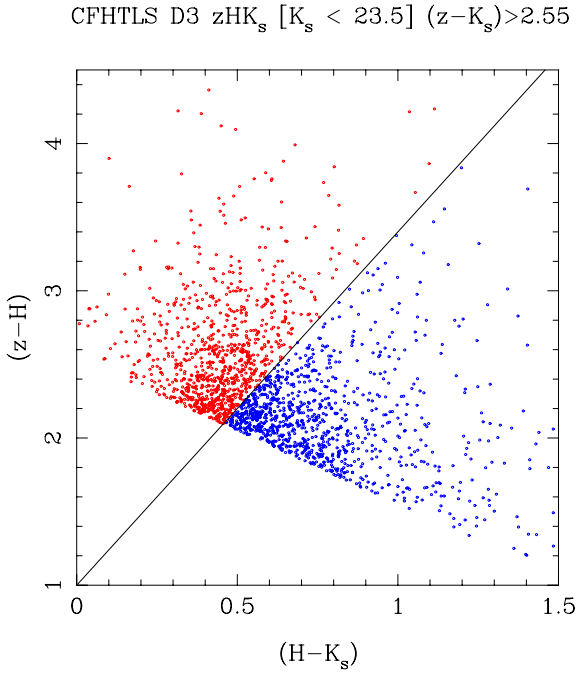

Figure 4. $(z - H)$ versus $(H - K_s)$ colours for those objects with $(z - K_s) > 2.55$ in CFHTLS Field D3 to $K_s < 23.5$. The blue points represent SF galaxies while the red points represent passive galaxies. The solid line separates the SF and passive regions described by equations (5) and (6). The diagonal cut-off in the lower part of the diagram reflects the $z - K_s > 2.55$ colour cut.

the z' and H filters. Therefore, we should be able to identify this feature using the $(z - H)$ versus $(H - K_s)$ colour–colour diagram (Fig. 3).

The passive/SF ambiguity exists for $(z' - K_s) > 2.55$ objects only, and so in Fig. 3 we plot only those models from the gzK_s diagrams (Fig. 1) that are above $(z - K_s) = 2.55$. As expected, the SF and passive models lie in different regions of Fig. 3 and thus provide us with the means to distinguish the two populations.

Note that for an SF galaxy, as age, dust and redshift are increased, the models shift parallel to the diagonal line shown in Fig. 3. This linear shift occurs because increasing dust will affect both colours by roughly the same amount and, moreover, the fact that the SF spectrum is not expected to have a break also ensures smooth evolution with redshift. In essence, SF galaxy spectra, even in the presence of dust, are essentially power laws at these wavelengths, ensuring their position in the lower-right panel of Fig. 1.

In contrast, for PE models, the presence of a spectral break results in a much stronger change between the $(z - H)$ and $(H - K_s)$ colours. As expected, models that represent PE galaxies lie on a different locus in Fig. 3, where they can be clearly separated from the CSF models. We adopt the solid black line in Fig. 3 as the division between models of SF and passive gzK_s-selected galaxies that have $(z - K_s) > 2.55$.

We then use the following criteria to select and classify $z \sim 2$ galaxies in our sample. First, as described in Section 3.2, we use equation (4) to select $z \sim 2$ galaxies regardless of their spectral type. Below $(z - K_s) = 2.55$, all objects selected using equation (4) are classified as SF $z \sim 2$ galaxies. Above $(z - K_s) = 2.55$, all galaxies selected using equation (4) are also deemed to be at $z \sim 2$, and are the classified as SF if

$$(z - H) \leq 2.4(H - K_s) + 1, \quad (5)$$

and as PE if

$$(z - H) > 2.4(H - K_s) + 1. \quad (6)$$

We call the star-forming objects thus selected 'SF-*gzHK*' galaxies, and the passively evolving ones 'PE-*gzHK*' galaxies. The models used in designing the above selection criteria are the same as those in the 'classic' BzK_s colour–colour cuts, and so we stress that the populations selected by our criteria are essentially the same as those selected using the 'classic' BzK_s technique.

Application of the above criteria to our photometric catalogues of Section 2 yields samples of $z \sim 2$ SF and PE galaxies in the CFHTLS Deep Fields. Their bulk properties are summarized in Table 1. An example of how our data looks for one of our deep fields (D3) in a $(z - H)$ versus $(H - K_s)$ colour–colour plot is presented in Fig. 4.

4 K_s-BAND GALAXY NUMBER COUNTS

In this section, we determine galaxy number counts for different populations of galaxies: SF and passive galaxies at $z \sim 2$ [as defined by equations (5) and (6)], as well as for all galaxies irrespective of redshift (equation 3). To do this, we count galaxies in 0.5 mag-wide total K_s magnitude bins and – because some faint galaxies can be undetected above night-sky fluctuations – apply incompleteness corrections determined from simulations.

Our incompleteness corrections use artificial objects added at random locations into the science images with empirically motivated morphological parameters. SF galaxies are assumed to be disc-like objects with effective radii in the range $1 \leq r_e \leq 3$ kpc (Yuma et al. 2011) while passive galaxies present a more compact morphology and effective radii in the range $3 \leq r_e \leq 6$ kpc (Mancini et al. 2010). The total (i.e. irrespective of redshift) galaxy number counts are corrected using morphologies that mimic the observed CFHTLS

Table 2. Adopted K_s-band completeness limits. Listed are bin centres of the faintest 0.5 mag-wide bins that are included in our analysis.

Population	D1	D2	D3	D4
All galaxies	24.0	23.5	24.0	24.0
SF galaxies	24.0	23.5	24.0	24.0
PE galaxies	24.0	23.0	24.0	23.5

galaxy population. Once artificial galaxies are added into an image, object finding with SExtractor is used to determine the recovery rate as a function of apparent magnitude.

Incompleteness corrections are typically of the order of ∼1.02 over $K_s = 17 - 22$ (AB) mag but become larger at fainter levels. We limit our analysis in magnitude bins where incompleteness corrections are smaller than a factor of 2. Table 2 lists our adopted completeness limits.

4.1 All galaxies irrespective of redshift

Galaxy number counts for all the galaxies in each field [selected using equation (3)] are shown in Fig. 5. The error bars for each field in this figure show $\sqrt{N}$ uncertainties. The filled black points represent a straight average between the four fields and their error bars represent their sum in quadrature of the individual fields' error bars.

We compare our results with those of other studies, including Lane et al. (2007), Hartley et al. (2008), Blanc et al. (2008) and McCracken et al. (2010). [We note that McCracken et al. (2010) use the same NIR data as we do, but their survey is limited to the D2/COSMOS field.] Key information on these surveys can be found in Table 3. We do not plot the results of earlier surveys (e.g. Kong et al. 2006; Hayashi et al. 2007) because they were limited in either depth or area and their results have been superseded by more recent work. As can be seen in Fig. 5, our results at faint magnitudes seem to be in good agreement with the results of the other studies. The small variations between our four fields, as well as between the various surveys, are most likely due to cosmic variance (i.e. variations in the galaxy number density due to small-scale inhomogeneities in the Universe).

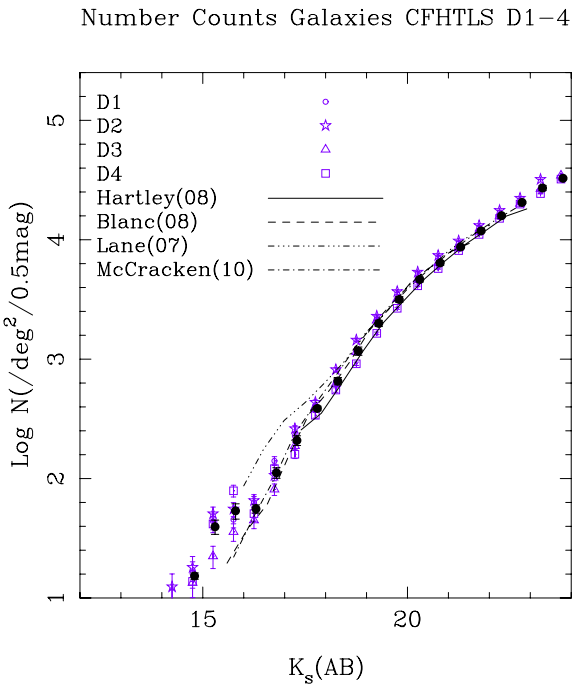

Figure 5. Number counts for K_s-selected galaxies (irrespective of redshift). Our results are in good agreement with other authors and their results of K_s-selected galaxies.

At the bright end ($K_s < 18$), there is significant scatter between surveys. Additionally, our counts exhibit a bump around $K_s = 15$, which could be attributed to a number of reasons. One could be merely due to how SExtractor detects and deals with bright objects. It should also be taken into account that at this bright end, our number counts are relatively low, giving large error bars. Results from Lane et al. (2007) also seem to exhibit a bump at bright magnitudes, while those of McCracken et al. (2010) do not, and the rest of the authors have not presented results at this bright end. Nevertheless, the variations at the bright end are not of great concern here since we are mainly interested in faint objects.

4.2 SF $z \sim 2$ galaxies

Fig. 6 shows galaxy number counts for $z \sim 2$ SF galaxies. Since many of our SF-$gzHK_s$ candidates are undetected in the g band (Section 3), we need to deal with potential low-redshift interlopers amongst the $z - K_s < 2.55$ objects (the $z - K_s > 2.55$ objects are all regarded to be at high redshift and their SF/PE nature is resolved using zHK_s colours alone). To address this interloper issue, Fig. 6 shows two extreme number count cases. The points show the number counts of $z - K_s < 2.55$ galaxies that are detected in the g band and hence known to fulfil the high-z colour selection criteria (in this case, we are rejecting from the sample any galaxy that was not detected in g). As such, the points represent a lower limit on the true number counts of SF galaxies. In particular, the black filled points represent the average of the lower limits set by our four deep fields. In contrast, the purple hatched region represents the full range of allowable number counts as it accounts for the g-band undetected objects, many of which could be low-redshift interlopers. The upper and lower limits of the cross-hatched regions thus represent the allowable range of SF galaxies. Note that this allowed range is quite narrow and thus we can claim to have constrained the number counts of SF galaxies quite well.

We compare our SF galaxy number counts with the counts presented by Blanc et al. (2008), Hartley et al. (2008), Lane et al. (2007) and McCracken et al. (2010). We do not show the $sBzK$ counts of Bielby et al. (2012), which are based on the same CFHT data as our work, since their use of traditional three-filter BzK selection in the presence of the relatively shallow CFHTLS g-band data can result in misclassifications of PE/SF galaxy spectral types at faint magnitudes. Our results for SF galaxies seem to be in good agreement with most authors except with Lane et al. (2007). Lane et al. (2007) attributed the differences between their number counts of SF galaxies and other authors such as Kong et al. (2006) to cosmic variance. However, cosmic variance between our four CFHT fields, each of which is similar in size to the field of Lane et al. (2007), is relatively small: it thus seems unlikely that the very high number counts of Lane et al. (2007) should be due to cosmic variance. Blanc et al. (2008) argue that the Lane at al. (2007) colour selection does not reproduce the standard BzK_s selection well and our cosmic variance analysis supports that conclusion.

Table 3. K_s magnitude limits and effective areas for the different authors presented to compare our results. Areas for these different authors are smaller than listed due to masking of bad regions. However, the area presented for this work, CFHTLS+WIRDS, is in fact the effective area of the survey after masking of bad regions.

Field	Mag lim K_s(AB)	Area (deg^2)	No. of fields
Lane et al. (2007)	22.50	0.55	1
Hartley et al. (2008)	23.00	0.63	1
Blanc et al. (2008)	21.85	0.71	2
McCracken et al. (2010)	23.00	1.89	1
This work (CFHTLS+WIRDS)	23.00	2.47	4

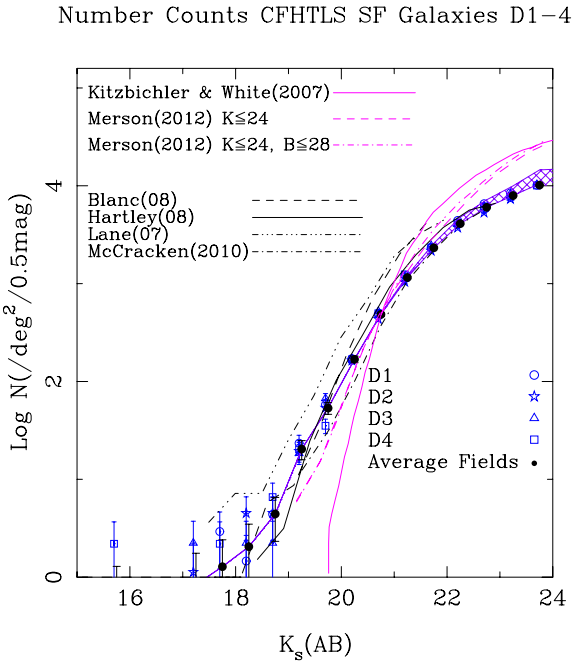

Figure 6. Galaxy number counts for SF galaxies. The open blue symbols represent our four Deep Fields D1–4, with error bars determined from Gaussian statistics. Also shown with filled black circles are galaxy number counts for the average of our four fields, with error bars calculated from the individual fields' error bars combined in quadrature. Both open blue symbols and black filled circles were shifted horizontally from the mid-point of the bin for clarity. As explained in the text, the hatched purple region represents upper and lower limits between our g-detected and g-undetected galaxies and thus marks the allowable range of SF galaxy number counts.

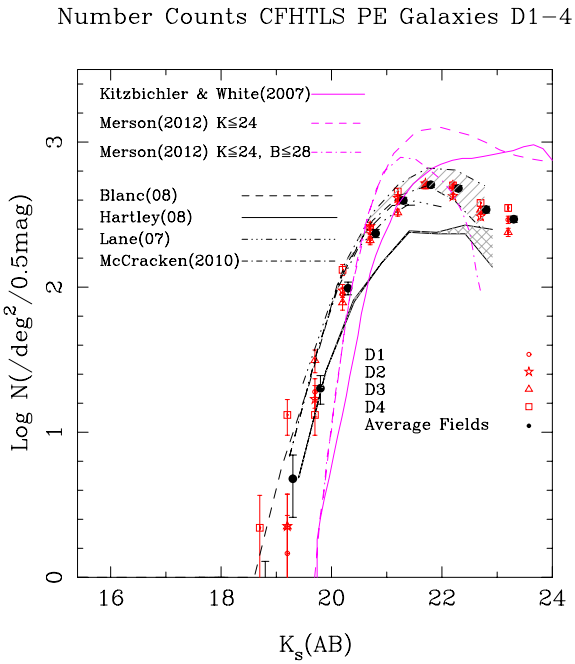

Figure 7. Galaxy number counts for $z \sim 2$ passive galaxies selected using the $gzHK_s$ selection criteria. The open red symbols represent our four Deep Fields D1–4. The error bars were determined from Gaussian statistics. Also shown with filled black circles are galaxy number counts for the average of our four fields, for which error bars represent the root-mean-square deviation. Both open red symbols and black filled circles were shifted horizontally from the mid-point of the bin for clarity.

4.3 Passive $z \sim 2$ galaxies

Galaxy number counts for $z \sim 2$ passive galaxies are shown in Fig. 7. As before, we compare our results with those of several different authors that used the BzK_s selection technique. For Hartley et al. (2008) and McCracken et al. (2010), we included a shaded area that represents their upper and lower limits. For Hartley et al. (2008), the upper limit represents the possibility that all of their non-detections in B and z' were in fact $pBzK$ galaxies. Although their lower limit exhibits a turnover in the number counts at faint magnitudes, once the upper limit is considered, there is no evidence for turnover in their number counts before their $K_s = 23$ limit.

For McCracken et al. (2010), the lower limit of their shaded region indicates galaxies that are unambiguously $pBzK$, while the upper limit also includes galaxies with ambiguous SF/PE classifications due to their lack of B-band detection. Even taking into account their worst case scenario, they observe a flattening of the number counts although within the limits the data are consistent with no turnover.

Our results seem to be in good agreement with most of the other studies, especially with McCracken et al. (2010). The only significant discrepancy is with Hartley et al. (2008). McCracken et al. (2010) suggested that the colour transformation used by Hartley et al. (2008) did not reproduce the classic BzK selection well, leading to discrepancies between these authors and other studies. We again do not show the results of Bielby et al. (2012) since their use of the classic three-filter BzK selection with the relatively shallow CFHTLS g-band data can lead to significant biases in their selection at fainter magnitudes.

4.4 Detailed comparisons

In Sections 4.1–4.3, we found that our results are in good general agreement with those of most other recent surveys. Our study's large total area, split over four independent sightlines, allows us to

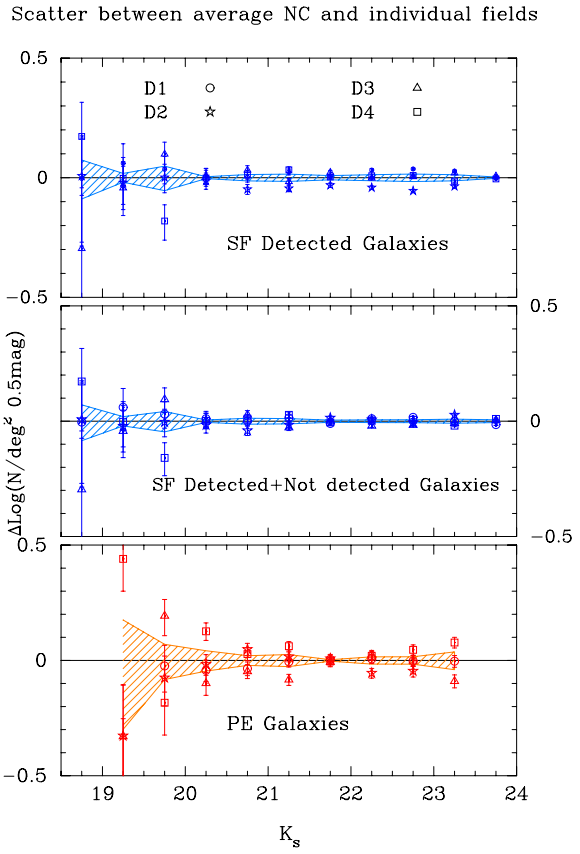

Figure 8. Scatter between our different populations and their respective average number counts. The top panel shows the scatter for only galaxies that were classified as SF and detected in g, while the middle panel also shows SF galaxies regardless of whether or not they were detected in g. The bottom panel shows the scatter for PE galaxies.

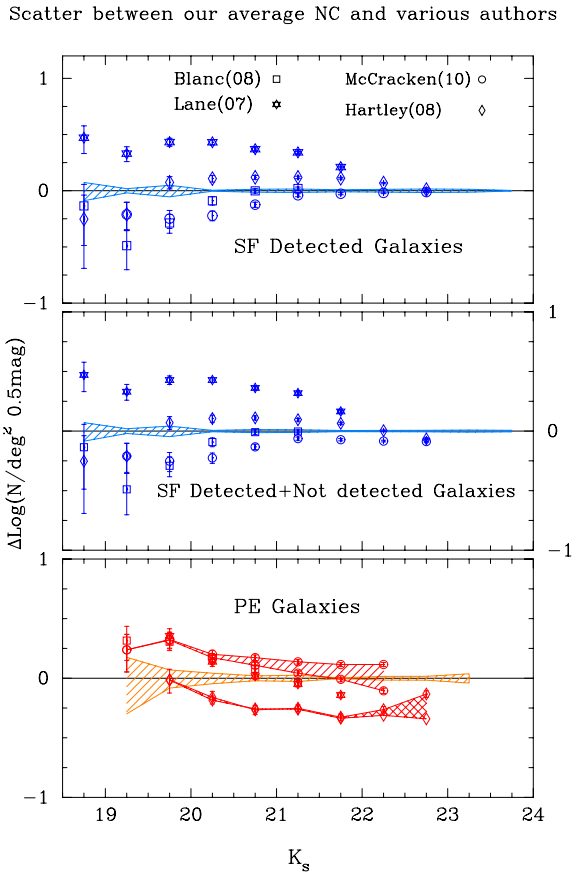

Figure 9. Scatter between our average number counts and those of various authors. The top panel shows the scatter for only galaxies that were classified as SF and detected in g, while the middle panel also shows SF galaxies regardless of whether or not they were detected in g. The bottom panel shows the scatter for PE galaxies. Following the representation given in Fig. 7, the shaded areas represent the upper and lower limits (see the text) of Hartley et al. (2008) (cross-hatched region) and McCracken et al. (2010) (hatched region).

carry out much more detailed comparisons, in particular focusing on the issue of cosmic variance in addition to purely systematic variations between different surveys. To do so, we will take the average counts in our four fields as baseline and then ask (i) how much field-to-field variation there is within our data? and (ii) how big are the differences between different studies?

Fig. 8 shows the residuals of our number counts after subtracting off the mean counts computed by averaging the results of the four fields. The shaded regions represent the uncertainty in the mean computed by summing the individual fields' uncertainties in quadrature. Except at the very brightest magnitudes, which are dominated by small number statistics, the field-to-field variance is quite small, though significant when compared to the error bars. In particular, the D2 (COSMOS) field shows signs of a deficit of $z \sim 2$ galaxies compared to our four-field average. Most significantly, here, the number of faint (K_s >22) passive galaxies is lower than the average by about 10 per cent. The number of g-detected SF galaxies is also low in D2, though the discrepancy for the SF object disappears once g-undetected galaxies are included. There are other departures from the average counts – e.g. the D4 field has a surplus of PE galaxies – but the deficits in D2 (COSMOS) are of particular note given the importance of this field in extragalactic studies (Scoville et al. 2007). We will touch on this issue again in Section 5 when we discuss the $z \sim 2$ LFs.

The observed field-to-field variance can be regarded as either due to large-scale structure present in the four fields ('cosmic variance') or systematic experimental variations such as photometric calibration errors, etc. Because any interfield differences cannot be smaller than that due to cosmic variance, field-to-field variance we observe puts an upper limit on the amount of cosmic variance present on the scales ∼0.5 deg^2.

Turning to variance between studies, in Fig. 9 we plot the residuals of various surveys' number counts after subtracting off the average of our study's four fields. As we mentioned before, all results are in broad agreement except for the SF galaxy counts of Lane et al. (2007) and the PE galaxies of Hartley et al. (2008). Examining the data more closely we see that there nevertheless exist systematic differences even between the other surveys. When comparing any two surveys, the offsets are often magnitude dependent and can range from zero to as much as ∼0.3 dex. Since cosmic variance is relatively small, as shown by the small field-to-field scatter among the four CFHT fields, the differences between surveys are likely to be due to systematic effects. In particular, although all surveys use *BzK*-like selection, they all rely on somewhat different filter sets and – hence – transformations to the original Daddi et al. (2004a) filter set. It is thus very likely that all these 'BzK' studies select somewhat different, if related, populations of galaxies, leading to the observed differences in number counts.

We conclude that cosmic variance in ∼0.5 deg^2 $z \sim 2$ surveys is relatively small in comparison to systematic calibration effects.

4.5 Comparison with models

Number counts from some semi-analytic models are also shown in Figs 6 and 7 using magenta lines.

The solid magenta lines represent models from Kitzbichler & White (2007) as presented by McCracken et al. (2010). In both figures, the Kitzbichler & White semi-analytic models overpredict the number of faint galaxies and underpredict the number of bright galaxies as compared with observational results.

Semi-analytic models from Merson et al. (2013) are shown as magenta dashed and dot–dashed lines. The dashed line represents model *BzK* galaxies brighter than $K_{\rm AB} \leq 24$. Although the number counts of SF galaxies show overall good agreement with observations at the bright end ($K_s \sim 20$), the model overpredicts the number of faint SF galaxies.

To assess the importance of a *B*-band depth in *BzK* selection, Merson et al. (2013) recalculated their predicted number counts of SF-*BzK*$_s$ and PE-*BzK*$_s$ assuming a *B*-band detection limit of $B_{\rm AB} = 28$ in addition to the original *K*-band limit of $K_{\rm AB} \leq 24$. These results are shown as dot–dashed magenta lines in Figs 6 and 7. As before, the predicted number counts are not in full agreement with the data, but the predictions for PE-*BzK*$_s$ galaxies are somewhat improved.

In light of the discussion in Section 4.4, we note that intersurvey differences are likely dominated by systematic uncertainties in, e.g. colour transformations. Such systematics likely also contribute to the disagreement between models and data, but given the size of this disagreement, it remains likely that the models do not yet capture all the relevant physics.

5 REST-FRAME *R*-BAND LFs

In this section, we measure and analyse the LF of passive and SF galaxies at $z \sim 2$.

5.1 Estimating the LF

We break the construction of the LF into three steps: (1) correction of the observed number counts for incompleteness, (2) determination of the survey effective volumes ($V_{\rm eff}$) and (3) conversion of apparent *K*-band to absolute *R*-band magnitudes. The first of these three steps, incompleteness correction, was already discussed in Section 4. The other two steps are described below.

For simplicity, we assume that our galaxies come from a well-defined redshift interval that can be described by a simple top-hat redshift selection function. The boundaries of this selection function are chosen based on examining the same models that we used in designing the colour–colour selection regions in Section 3. For concreteness, for SF galaxies we adopt the 100 Myr continually SF model with $E(B-V) = 0.2$ and this gives $V_{\rm eff} = 1.69 \times 10^7\,{\rm Mpc}^3\,{\rm deg}^{-2}$. Other reasonable combinations of age and extinction give values that are up to ∼1.5 times higher or lower than this fiducial. For passive galaxies, we adopt the 1 Gyr-old single-burst model with no dust, which results in $V_{\rm eff} = 1.77 \times 10^7\,{\rm Mpc}^3\,{\rm deg}^{-2}$. Older models give $V_{\rm eff}$ up to ∼1.3 times larger than this fiducial value and younger models give $V_{\rm eff} \sim 3$ times lower for young ($\sim 10^{8.5}$ Gyr) instantaneous bursts.

Next, in the usual way (see, e.g., Lilly et al. 1995; Sawicki & Thompson 2006), absolute *R*-band magnitudes are calculated from the observed *K*-band using

$$M_R = m_{\lambda_{\rm obs}} - 5\log\left(\frac{D_L}{10\,{\rm pc}}\right) + 2.5\log(1+z) + \left(m_R - m_{\lambda_{\rm obs}/(1+z)}\right). \quad (7)$$

Here D_L is the luminosity distance and the last term is the *k*-correction colour between the rest-frame *R* and observed K_s bands. We assume $z = 2$ for the calculation and note that because of our choice to work at the rest-frame *R*, the *k*-correction colour term will be small and insensitive to the assumed galaxy spectral energy distributions (SED). Assuming here that our galaxies are at $z = 2$ may introduce two biases: first, if the median redshift of our sample differs from $z = 2$, the overall magnitude calibration of the LF will be also offset. Secondly, because our $z \sim 2$ samples contain galaxies over a range of redshifts, the LF will suffer a degree of smearing along the magnitude direction. However, these effects are not likely to dramatically affect our LF measurement: taking $z = 1.5$ or 2.5 instead of $z = 2$ gives a systematic offset of ∼±0.5 mag and this is small compared to the features in the LF that we will be discussing in the next section. Furthermore, the assumption that the median redshift of our sample lies at $z \sim 2$ has been supported by previous studies (e.g. Daddi et al. 2004a; Reddy et al. 2005; Hayashi et al. 2007; Pérez-González et al. 2008).

Using the steps described above, we convert the incompleteness-corrected $\phi_f\,(m)$ number count values determined in Section 4 to the rest-frame *R*-band LF $\phi_f\,(M_R)$. We plot them in Fig. 10, where blue is used to identify SF galaxy LFs and red represents PE ones.

5.2 Analysis of the LFs

The LF data are fitted using the Schechter (1976) LF parametrization

$$\phi_{\rm model} = \phi^* 0.4\ln(10)\{{\rm dex}\left[0.4(M^* - M)\right]\}^{(\alpha+1)} \times \exp(-10^{0.4(M^*-M)}), \quad (8)$$

where only points fainter than $M_R = -25$ were used in the fit. The best-fitting functions are plotted as red and blue curves in Fig. 10, the best-fitting Schechter parameter values are given in Table 4, and the error contours for the Schechter parameters for the SF and passive populations are shown in Fig. 11.

The faint-end slope for SF galaxies is $\alpha = -1.41^{+0.05}_{-0.04}$ or $\alpha = -1.45^{+0.05}_{-0.04}$ if *g* non-detections are also included in the fit. Combining these two results gives $\alpha = -1.43 \pm 0.02^{+0.05}_{-0.04}$ (systematic and random uncertainties, respectively). It is worth noting that our SF galaxy faint-end slope is in very good agreement with the BX galaxy, $\alpha = -1.47^{+0.24}_{-0.21}$, of Sawicki (2012b). While the BX and SF-*BzK* populations are necessarily somewhat different, both these techniques aim to select SF galaxies at $z \sim 2$ and do give significant overlap (e.g. Reddy et al. 2005). The similarity between the observed BX and SF-*BzK* faint-end slopes, while not surprising, is reassuring.

Turning to PE galaxies, our PE galaxy faint-end slope $\alpha = -0.12^{+0.16}_{-0.14}$ is in good agreement with the determinations of the low-mass end of the $z \sim 2$ PE galaxy SMFs (e.g. Wuyts et al. 2008; Kajisawa et al. 2011), but our α measurement is much better constrained than in those earlier studies, owing to our large ∼5000-object sample of $z \sim 2$ passive galaxies. It is now clear that the numbers in the faint/low-mass end of the PE-*BzK* galaxy

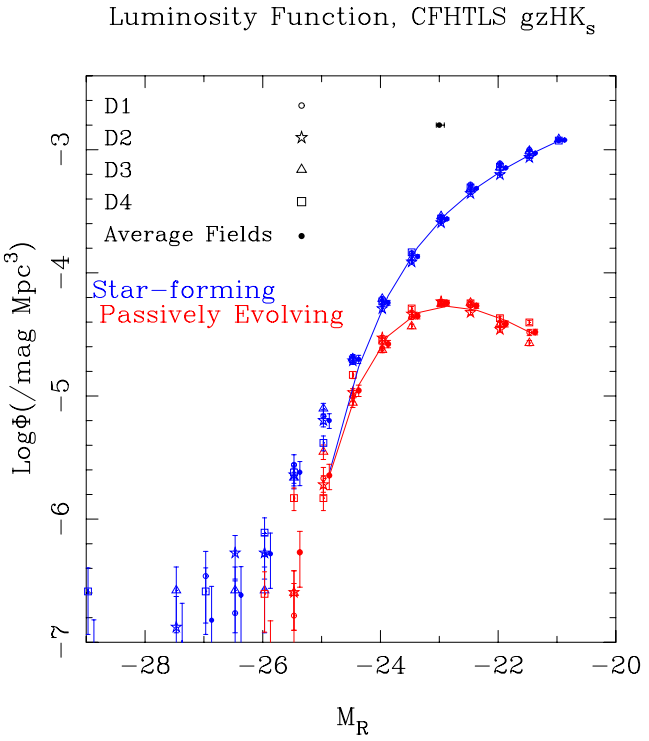

Figure 10. Rest-frame R-band LFs for $z \sim 2$ passive (red symbols) and SF (blue) galaxies. Results from each Deep Field are represented with a different open symbol, while the averaged results are shown with filled points. Points have been shifted horizontally from the bin mid-point for clarity. The error bars for individual fields are $\sqrt{N}$, while the error bars for the average fields represent their sum in quadrature. The best-fitting Schechter functions are shown as blue and red solid lines. In the upper part of the figure, the horizontal error bar is an estimate between our best guess in absolute magnitude and the difference between this best guess and our upper and lower limits at $z \sim 2$.

population at $z \sim 2$ trend strongly downwards, with a steeply declining slope as is also seen for passive galaxies at lower redshifts. The most common passive galaxy at $z \sim 2$ has $M_R \sim -23$, an issue that we will revisit in Section 6 where we examine galaxy stellar masses.

With the Schechter fit parameters in hand, integrating the Schechter function gives the sum of all the light from all galaxies in a unit of volume:

$$\rho_L = \int_0^\infty L\phi\,(L)\,\mathrm{d}L = \phi^* L^* \Gamma\,(\alpha + 2)\,, \qquad (9)$$

where $\Gamma(x) = \int_0^\infty t^{x-1}\mathrm{e}^{-t}\mathrm{d}t$ is the usual gamma function. Column 6 of Table 4 lists the rest-frame R-band luminosity densities in our four fields. The integrated luminosity density does not vary significantly from field to field. Typical departures from the averaged field values are $\lesssim$10 per cent, which is entirely within the error budget. However, these luminosity density values hide underlying differences between fields in the shapes of the LFs. As with the number counts (Section 4.4), there are field-to-field differences in the LF shapes (Fig. 10) and these differences are also reflected in differences in the Schechter function parameters (Fig. 11). In particular, the D2 (COSMOS) field is especially anomalous: there is a deficit of faint PE galaxies in this field compared to the average, and this is reflected in a shallower value of the faint-end slope parameter α (see the bottom-left panel of Fig. 11). Similarly, the LF of SF galaxies in the D2 field also appears significantly different from the average LF and these differences would be increased if we were to exclude the potentially anomalous D2 field from that average. The observed field-to-field variation is not large – the deficit of faint galaxies in D2 is ∼10 per cent compared to the average – and is likely consistent with fluctuations due to large-scale structures. However, the fact that the D2 (COSMOS) field is anomalous is notable because of the importance of this extremely well studied field in galaxy formation studies.

Our LF for passive galaxies shows a turnover (rather than just a flattening), with the peak at $M_R \sim -23$. This implies that the passive galaxy population at $z \sim 2$ is dominated by bright (massive)

Table 4. Schechter function fits and luminosity densities for the four CFHTLS/WIRDS Deep Fields. Note: ρ_L is at rest-frame R and is given in logarithmic units of erg s^{-1} Hz^{-1} Mpc^{-3}.

Population	Field	M^*	$\log_{10}\phi^*$ (Mpc^{-3})	α	ρ_L
g-detected SF	Average	$-23.15^{+0.09}_{-0.11}$	$-3.19^{+0.05}_{-0.06}$	$-1.41^{+0.05}_{-0.04}$	$26.90^{+0.07}_{-0.08}$
	D1	$-23.00^{+0.09}_{-0.01}$	$-3.08^{+0.05}_{-0.05}$	$-1.32^{+0.04}_{-0.05}$	$26.89^{+0.06}_{-0.07}$
	D2	$-23.33^{+0.13}_{-0.13}$	$-3.34^{+0.08}_{-0.09}$	$-1.52^{+0.07}_{-0.07}$	$26.90^{+0.11}_{-0.13}$
	D3	$-23.17^{+0.09}_{-0.12}$	$-3.19^{+0.05}_{-0.07}$	$-1.42^{+0.04}_{-0.05}$	$26.91^{+0.07}_{-0.09}$
	D4	$-23.16^{+0.1}_{-0.08}$	$-3.18^{+0.06}_{-0.05}$	$-1.39^{+0.05}_{-0.04}$	$26.90^{+0.07}_{-0.07}$
g-detected and not detected SF	Average	$-23.08^{+0.10}_{-0.09}$	$-3.11^{+0.06}_{-0.05}$	$-1.45^{+0.05}_{-0.04}$	$26.98^{+0.08}_{-0.07}$
	D1	$-22.99^{+0.09}_{-0.09}$	$-3.04^{+0.04}_{-0.06}$	$-1.38^{+0.04}_{-0.05}$	$26.96^{+0.06}_{-0.08}$
	D2	$-23.27^{+0.12}_{-0.12}$	$-3.24^{+0.08}_{-0.08}$	$-1.62^{+0.07}_{-0.06}$	$27.08^{+0.11}_{-0.13}$
	D3	$-23.22^{+0.11}_{-0.09}$	$-3.20^{+0.06}_{-0.06}$	$-1.52^{+0.05}_{-0.04}$	$27.00^{+0.08}_{-0.09}$
	D4	$-23.15^{+0.09}_{-0.10}$	$-3.14^{+0.04}_{-0.06}$	$-1.47^{+0.04}_{-0.05}$	$26.99^{+0.06}_{-0.08}$
Passive	Average	$-22.98^{+0.16}_{-0.14}$	$-3.80^{+0.03}_{-0.04}$	$-0.12^{+0.16}_{-0.14}$	$26.02^{+0.06}_{-0.08}$
	D1	$-22.90^{+0.14}_{-0.16}$	$-3.80^{+0.03}_{-0.04}$	$-0.08^{+0.16}_{-0.16}$	$25.99^{+0.07}_{-0.06}$
	D2	$-22.84^{+0.12}_{-0.14}$	$-3.80^{+0.02}_{-0.02}$	$0.14^{+0.20}_{-0.17}$	$26.01^{+0.07}_{-0.07}$
	D3	$-22.86^{+0.18}_{-0.16}$	$-3.82^{+0.03}_{-0.04}$	$-0.04^{+0.20}_{-0.16}$	$25.96^{+0.08}_{-0.09}$
	D4	$-23.02^{+0.12}_{-0.12}$	$-3.77^{+0.03}_{-0.04}$	$-0.18^{+0.12}_{-0.14}$	$26.06^{+0.06}_{-0.07}$

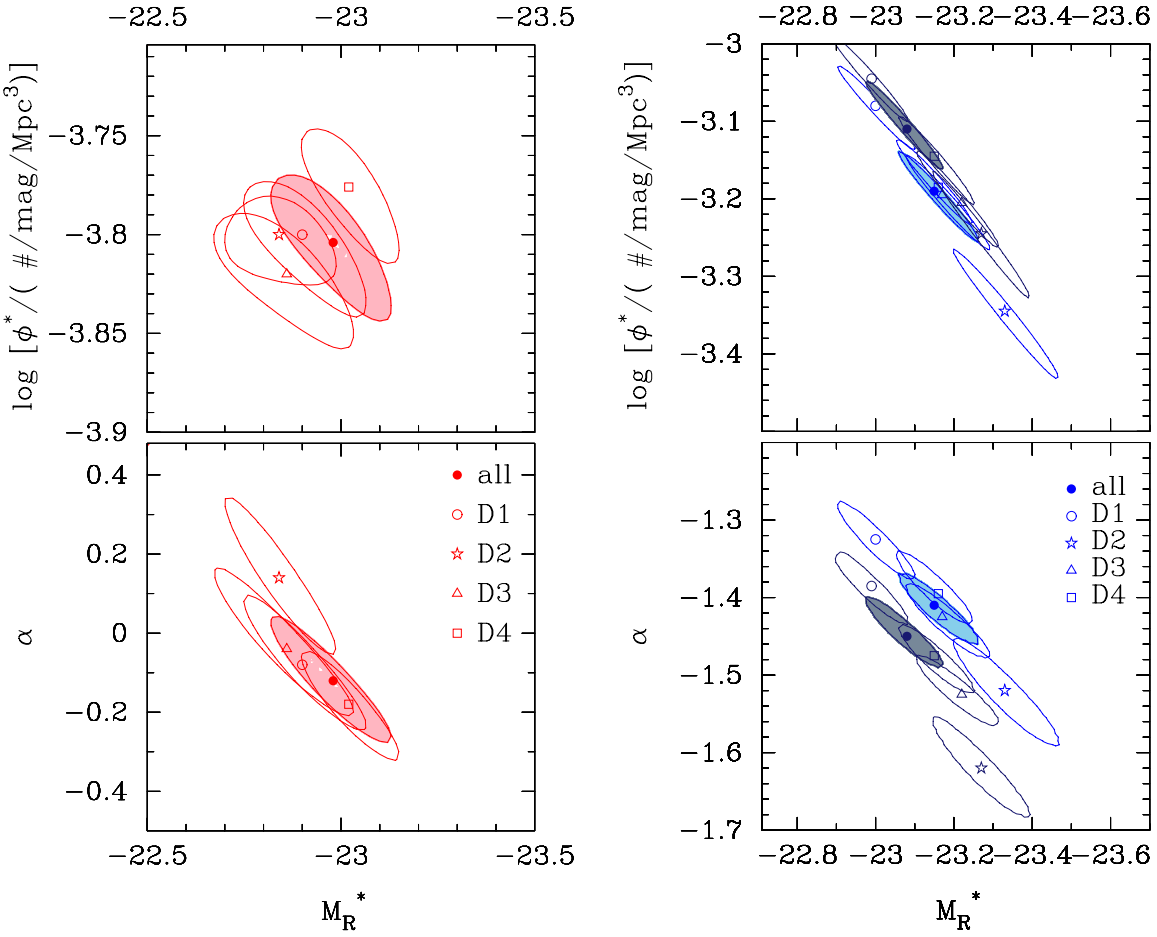

Figure 11. Confidence regions (1σ) on the Schechter LF parameters for the PE (left) and SF (right) populations. The filled symbols and shaded contours denote the averages over the four fields. In the right panels, SF galaxies detected in the *g* band are represented in lighter blue while dark blue is for galaxies that were classified as SF regardless of whether or not they were detected in the *g* band.

objects, a phenomenon that is consistent with the 'downsizing' scenario. Downsizing, as introduced by Cowie et al. (1996), implies that star formation stops in massive systems first and in lower mass systems later. Our observations are consistent with the downsizing scenario because if we interpret the rest-frame *R*-band luminosity as a surrogate for the stellar mass of a galaxy, then at the low-mass end most galaxies are still forming stars, while at the massive end passive and SF galaxies are present in roughly equal numbers. It is important to note that both a turnover and a simple flattening in the LF are consistent with downsizing. However, a turnover – which is now observed in the data – represents a much more interesting scenario because it suggests that there is a characteristic luminosity (i.e. mass) at which galaxies are most likely to evolve into passive systems. We examine this issue further in the next section.

6 STELLAR MASS FUNCTIONS

Rest-frame *R*-band light in galaxies is generated in large measure by the long-lived low-mass stars that in stellar populations originating from reasonable IMFs can be expected to contain most of a galaxy's stellar mass. Via a simple light-to-mass conversion, rest-frame *R*-band luminosities can thus be used to estimate stellar masses of distant galaxies, and, consequently, rest-frame *R*-band LFs can be used as a proxy for SMFs.

Using this approach, in this section we make a straightforward estimate of the $z \sim 2$ SMFs from the LFs determined in Section 5. The conversion from the *R*-band luminosity is more straightforward for PE objects than it is for SF ones, and so we focus our analysis on the PE SMF, only briefly touching on the SF SMF.

6.1 From LF to SMF

We apply a very simple procedure to convert the LFs we determined in Section 5 to SMFs, treating the PE and SF conversions separately.

6.1.1 PE galaxies

For the PE galaxy population, we derive the light-to-mass conversion based on the luminosity of a $z = 2$, 700 Myr-old dust-free SSP from the Bruzual & Charlot (2003) model library. This simple model is consistent with the definition of PE BzK_s and $gzHK_s$ galaxies (Daddi et al. 2004a and also Section 3). In performing stellar mass estimates, it is important to account for stellar mass returned to the ISM by mechanisms such as stellar winds and supernova explosions, and for our 700 Myr-old SSP this returned fraction is 23 per cent [see the models of Bruzual & Charlot (2003)]. This light-to-mass conversion is sensitive to the assumed age of the stellar population – for example, a 2 Gyr-old SSP would give a stellar mass that is approximately two times heavier than what we assume; however, such a 2 Gyr stellar population, observed at $z = 2$, would

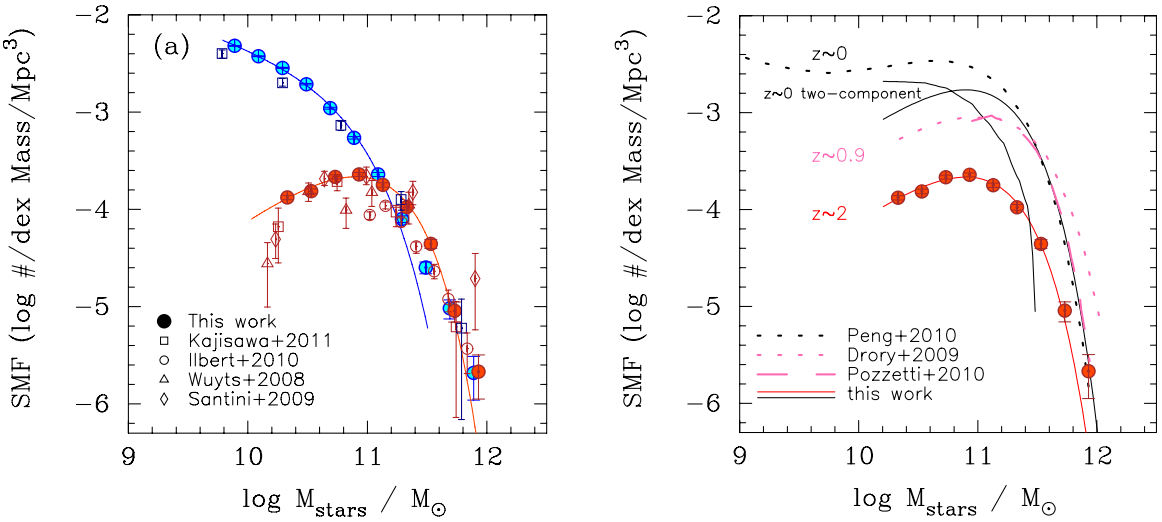

Figure 12. SMFs. The left-hand panel shows the $z \sim 2$ SMFs by galaxy type and in comparison with some previous studies. Some of the data points have been slight offset horizontally for clarity. The most common PE galaxy at $z \sim 2$ has a stellar mass of $\sim 10^{11}$ M$_\odot$ (Salpeter IMF). The right-hand panel shows the time evolution of the mass functions of PE galaxies. The two solid black curves, labelled '$z \sim 0$ two-component', represent the observed $z \sim 2$ SMF scaled up uniformly by a factor of 8 and the residual of subtracting that scaled $z \sim 2$ SMF from the observed $z \sim 0$ SMF. It thus appears plausible that a population of massive PE galaxies builds up uniformly in number, starting already before $z \sim 2$ and continuing to the present day. A time-invariant peak mass of $\sim 10^{11}$ M$_\odot$ is a hallmark of this build-up.

have to have formed at $z \sim 4.8$ and given the rapid factor of $\sim$10 growth in the stellar mass density of the Universe between $z \sim 5$ and $z \sim 2$ (e.g. Elsner, Feulner & Hopp 2008; Pérez-González et al. 2008; Yabe et al. 2009; Sawicki 2012a), it seems unlikely that many objects in our population of the $z \sim 2$ PE galaxies would have been already quiescent as early as $z \sim 5$. Conversely, galaxies with stellar populations significantly younger than our assumed 700 Myr cannot be considered to be truly quiescent yet by our definition, and so we settle on 700 Myr as a reasonable age that is also consistent with the classic definition of BzK_s galaxies (Daddi et al. 2004a).

Bearing in mind caveats regarding the simplicity of our light-to-mass conversion, we convert our observed $z \sim 2$ PE galaxy LF to a PE galaxy SMF. We show the result for our averaged fields (filled red points) in the left-hand panel of Fig. 12, along with our Schechter function fit to the data (red curve). The PE galaxy SMF at $z \sim 2$ has a steeply rising massive end and a declining low-mass end. The peak of the SMF, which corresponds to the mass of the most common PE galaxy at $z \sim 2$, is at $\sim 10^{11}$ M$_\odot$. The open red symbols in Fig. 12 show previous determinations of the PE SMF at $z \sim 2$ (Wuyts et al. 2008; Santini et al. 2009; Ilbert et al. 2010; Kajisawa et al. 2011) which we transformed, when necessary, to our adopted Salpeter (1955) IMF. Our PE galaxy SMF agrees well with these earlier determinations of the PE MF, but our sample contains many more objects and thus has much better statistics than these earlier studies.

6.1.2 SF galaxies

The light-to-mass conversion for SF galaxies is more uncertain than that for PE systems because of the uncertainties about their star formation histories (SFHs; we assume a constant SFR but in practice SFHs could be decreasing, increasing or variable with time) and interstellar extinction (we assume constant extinction whereas in practice extinction at $z \sim 2$ is a function of galaxy luminosity; Sawicki 2012b). Despite these issues, we proceed by adopting the 200 Myr-old, CSF Bruzual & Charlot (2003) stellar population with $E(B - V) = 0.3$. Our resulting SF galaxy SMF, shown with filled blue points in Fig. 12, is a reasonable match to that determined for $z \sim 2$ (Kajisawa et al. 2011) using full multiwavelength SED fitting applied to the deep observations of the Great Observatories Origins Deep Survey-North (GOODS-N) region. However, because of the higher systematic uncertainties associated with the SF galaxy SMF, in the next section we focus primarily on discussing the SMF of the PE systems, touching on SF galaxies only briefly at the end.

6.2 The non-evolving shape of the PE SMF

In the right-hand panel of Fig. 12, we compare our $z \sim 2$ PE galaxy SMF with SMFs observed at lower redshifts. The two $z \sim 0.9$ SMFs are both from data in the COSMOS field, one derived using a spectroscopic sample (Pozzetti et al. 2010), the other using a large photometric redshift one (Drory et al. 2009); the local PE galaxy SMF is from the analysis of SDSS data by Peng et al. (2010). All are plotted on a common Salpeter IMF scale.

The shape of the $z \sim 2$ PE galaxy SMF is remarkably similar to that at $z \sim 0.9$. In common with $z \sim 0.9$ observations, the $z \sim 2$ has a steeply rising massive end, a peak around 10^{11} M$_\odot$ and a declining low-mass end, although the overall normalization in number density is approximately four times higher at $z \sim 0.9$ than it is at $z \sim 2$. This remarkable similarity of the shape between $z \sim 2$ and $z \sim 0.9$, with just a shift of a factor of 4 in normalization across all masses, suggests that the same physical process may be responsible for forming the PE galaxy SMF that is seen at $z \sim 2$ as that at $z \sim 0.9$. In this scenario, the population of PE galaxies grows at a rate that gives a uniform increase of a factor of 4 in number, independent of mass.

The $z \sim 0$ PE galaxy SMF has been measured by numerous authors using SDSS data (e.g. Bell et al. 2003; Baldry et al. 2008; Peng et al. 2010), and in Fig. 12 we use the black curve to show the Peng et al. (2010) result. The overall shape of the $z \sim 0$ PE galaxy SMF is different from that at the earlier epochs: while the steep massive end is also present at $z \sim 0$, the decline in number density towards lower masses is not as steep as at higher redshifts and there is also a reversal and a raise at very low masses (below $\sim 10^{9.7}$ M$_\odot$).

Nevertheless, the $z \sim 0$ SMF shows a local maximum at $\sim 10^{10.6}\,M_\odot$, and this peak mass is similar to the mass of the $\sim 10^{11}$ peak at earlier times.

As mentioned earlier, it appears that evolution of the population of massive galaxies is consistent with simple number density increase between at least $z \sim 2$ and $z \sim 0.9$. It is then interesting to consider whether this simple number density growth of massive galaxies may also continue to $z \sim 0$. We do this by subtracting a high-mass component from the observed SDSS $z \sim 0$ SMF that is identical in shape to the $z \sim 2$ SMF and only differs from it in normalization. Doing so is similar to fitting two Schechter functions to the $z \sim 0$ SMF, but rather than allowing all the parameters to vary, here we fix the shape (i.e. $M^*_{\rm stars}$ and α) of the high-mass Schechter function, changing only its ϕ^*. The result is shown in Fig. 12 using the two black curves, one of which is the scaled-up $z \sim 2$ SMF and the other the residual of its subtraction from the SDSS data. Here we fixed the $z \sim 0$ normalization of the $z \sim 2$ SMF at eight times that observed at $z \sim 2$, although – given the extreme steepness of the high-mass end – a range of scaling factors result in reasonable results. It is clear from Fig. 12 that a high-mass component identical (except for its numerical normalization) to that seen at $z \sim 2$ can be present in the $z \sim 0$ SMF, leaving a second, low-mass Schechter component not seen at higher redshifts. It thus seems possible that a universal mechanism for the formation of high-mass PE galaxies is in action over a large range of redshifts, producing an ever growing, but self-similar PE galaxy SMF by simply adding new PE galaxies at a rate that only depends on their stellar mass. Direct evidence for this lies in the similarity between the PE galaxy SMFs at $z \sim 2$ and $z \sim 0.9$, while the possibility of the $z \sim 0$ SMF containing a scaled-up high-mass component extends this argument to the present epoch.

The SMF growth process described above is consistent with the mass-quenching scenario of Peng et al. (2010). In this mass-quenching model, the shutdown of star formation in massive galaxies turns SF galaxies into quiescent ones which then 'precipitate' on to the PE galaxy SMF at a rate that changes with time but does not vary strongly with galaxy mass. Peng et al. show evidence for this scenario between $z \sim 0$ and $z \sim 1$ (when the Universe was about half of its present age). Our data show that if such a process is indeed in operation, then it has already left its imprint at $z \sim 2$ ($\sim$10 Gyr ago, when the Universe was only a quarter of its present age). Furthermore, given that the PE galaxy SMF already has its characteristic shape at $z \sim 2$, the process must have already been in operation at even earlier epochs.

In the Peng et al. (2010) model, quiescent galaxies form from SF ones by two mechanisms: mass quenching and environmental quenching. In their analysis, environmental quenching is not expected to produce significant numbers of PE galaxies until low redshift. Consequently, unlike at low redshifts, where both mechanisms have contributed to the PE population, at high redshifts we can expect to be observing the pure population of mass-quenched galaxies, uncontaminated by environmentally quenched objects. This indeed appears to be the case if we interpret the single Schechter function shape of the $z \sim 2$ (and $z \sim 0.9$) PE galaxy SMF as due to the single process of mass quenching. The dominance of mass quenching at $z \sim 0.9$–2 (and likely earlier) opens the intriguing possibility of studying this quenching mechanism in isolation from other effects.

Peng at al. (2010) illustrate their proposed quenching scenario with a model of the fraction of galaxies that are passive (the 'PE fraction'). In Fig. 13, we reproduce their PE fraction curves for $z \sim 2$ where, unlike at low redshifts, mass quenching is expected to be the sole important quenching mechanism. One consequence of

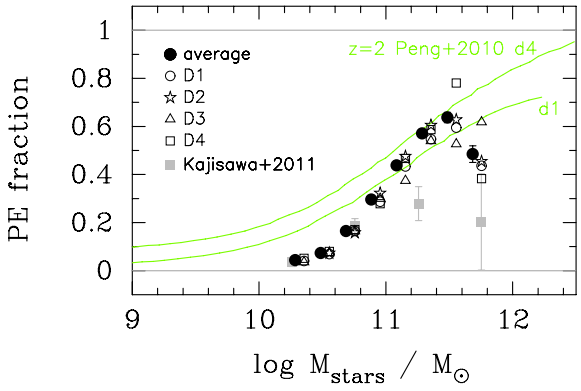

Figure 13. The fraction of galaxies that are PE at $z \sim 2$. Some of the CFHT points have been offset for clarity. The green curves show the $z \sim 2$ models of Peng et al. (2010) for the densest (d4) and least dense (d1) quartiles.

the dominance of mass quenching over environmental quenching at high redshifts is that the PE fraction is expected to be relatively insensitive to environment. Consequently, unlike at lower redshifts, their models for $z \sim 2$ are relatively insensitive to the local density of galaxies – shown here for their lowest (d1) and highest (d4) density quartiles – and we can compare the models with our data without concern for environment, which would be difficult to characterize given our lack of spectroscopic redshifts.

Our data, shown with black points in Fig. 13, are calculated by dividing the PE galaxy SMF by the sum of the PE and SF galaxy SMFs. The data show a trend that is qualitatively similar to the models: a low PE fraction at low masses, rising steeply to higher masses. A similar trend is seen in the data of Kajisawa et al. (2011), though with larger uncertainties and a shallower rise at high masses compared to that observed by us. The agreement between the data and the models shown here is only qualitative. However, it should be kept in mind that a range of effects may contribute to the discrepancy, such as differences in definitions of PE and SF galaxies between the data and the models and the systematic uncertainties in our light-to-mass conversions, particularly for the SF galaxies. We conclude that, qualitatively at least if not yet in detail, at the $z \sim 2$ epoch where mass quenching is expected to dominate the PE population, the observed PE fractions are in agreement with the scenario of Peng et al. (2010).

7 SUMMARY AND CONCLUSIONS

The popular BzK_s technique (Daddi et al. 2004a) gives the most complete way to select and classify galaxies at $z \sim 2$ that is based only on colour–colour cuts from three different broad-band filters. It provides the opportunity to study galaxy evolution in two populations distinguished by their modes of star formation: currently SF as well as passive and hence SF in the past. Our adaptation of this technique, combined with the large effective areas (0.4–0.9 deg^2 each for a total of 2.5 deg^2) and independent lines of sight of the four Deep Fields in the CFHTLS, allowed us to construct and study a large sample of SF and passive galaxies in four causally independent regions of the $z \sim 2$ Universe.

In our work, we first adapted the BzK_s technique to the CFHTLS+WIRDS gzK_s filter set and used it to select $\sim$40 000 $z \sim 2$ galaxies brighter than $K_{\rm AB} = 24$. Because the CFHTLS g-band data are not deep enough to reliably classify the faint galaxies in this $z \sim 2$ sample, we then applied a second colour criterion which uses the H filter together with the gzK_s to classify our $z \sim 2$ galaxies

into SF and passive objects. This $gzHK_s$ classification is entirely analogous to that given by the BzK_s criteria, allowing us to obtain a sample of ∼5000 $z \sim 2$ galaxies (to $K_{AB} = 23$) that is selected using essentially the popular BzK_s approach. This forms the largest sample to date of galaxies assembled and classified using BzK-like selection and allows the most precise measurement of their number counts, rest-frame R-band LFs and SMFs.

Based on the analysis of these data, our main findings are as follows.

(i) *Number counts and selection effects:* our number counts for both SF and passive $z \sim 2$ galaxies are in good agreement with those of most recent large-area studies that use BzK_s-classified samples (Blanc et al. 2008; McCracken et al. 2010). However, for SF galaxies our results are significantly lower than those obtained by Lane et al. (2007), and for PE galaxies they are higher than those of Hartley et al. (2008). Because the differences between our four large fields are relatively minor (see below), these discrepancies are unlikely to be due to cosmic variance unless the UKIRT Infrared Deep Sky Survey (UKIDSS) Ultra-Deep Field studied by Hartley et al. and Lane et al. is anomalous in the extreme. Instead, the number count differences are more likely due a mismatch between the Hartley et al. and Lane et al. definitions of passive and SF BzK_s galaxies compared to the 'standard' Daddi et al. (2004a) BzK_s system. These differences highlight the fact that classification into passive and SF objects is relatively arbitrary and can result in significant discrepancies in results between different studies unless care is taken to achieve consistency in object classification. It is likely that all 'BzK_s' studies select somewhat different, if related, populations. Differences between populations selected using diverse methods (colour–colour selection, photometric redshifts, morphologies, etc.), as well as those from simulations or theoretical work, are likely to be even larger.

(ii) *LFs:* the passive galaxy LF exhibits a clear peak at $M_R = -23$ and a declining faint-end slope with $\alpha = -0.12^{+0.16}_{-0.14}$. This measurement presents the clearest evidence to date of a turnover in the LF of $z \sim 2$ passive galaxies selected using a BzK_s-like technique. In contrast to the passive galaxies, the LF of SF galaxies is characterized by a steep faint-end slope, $\alpha = -1.43 \pm 0.02(\text{systematic})^{+0.05}_{-0.04}(\text{random})$. This is similar to the steep faint-end slope seen among the BX-classified $z \sim 2$ galaxies (Sawicki 2012b).

(iii) *Cosmic variance:* the details of both the number counts and LFs are somewhat sensitive to cosmic variance even in our large, ∼0.5 deg^2, fields. In particular, the D2 field (which is in the popular COSMOS survey area) yields LFs that are the most discrepant from the mean. The differences are not large – the differences in number counts among our ∼0.5–1 deg^2 fields are typically <25 per cent for PE galaxies and even less for SF ones. Nevertheless, we should continue to keep cosmic variance in mind, even when dealing with large fields, particularly as we attempt to move towards more and more precise measurements of various observational quantities.

(iv) *SMFs:* our rest-frame R-band LFs sample the low-mass stars that contain most of these galaxies' mass, and so we use them to estimate the $z \sim 2$ SMFs. These SMFs are most robust for PE galaxies (which can be assumed to have little dust and relatively simple SFHs) and so this is where we focus our analysis. The $z \sim 2$ PE galaxy SMF has a steeply rising high-mass end and a declining low-mass end, with a turnover at $M_{\text{stars}} \sim 10^{11}\,\text{M}_\odot$, the mass of the most common PE galaxy at $z \sim 2$. This picture is consistent with previous $z \sim 2$ studies but has much better statistics. The position of the $M_{\text{stars}} \sim 10^{11}\,\text{M}_\odot$ turnover and the overall shape of the PE galaxy SMF at $z \sim 2$ are very similar (except for its normalization, which is approximately four times lower) to that at $z \sim 0.9$. We also show that it is plausible that the $z \sim 0$ PE galaxy SMF may contain a subpopulation similar to that seen at higher redshifts. This similarity between the PE galaxy SMF shapes over the $z \sim 2$–0.9, and possibly also down to $z \sim 0$, suggests that a universal mechanism for the formation of high-mass PE galaxies is in action at a wide range of cosmic epochs. This mechanism, which could be related to the mass-quenching scenario proposed by Peng et al. (2010), appears to have already been in operation *before* $z \sim 2$ in order to produce the observed PE galaxy SMF by that epoch.

As summarized above, our study suggests the existence of a galaxy quenching mechanism that may be universal in time over at least 75 per cent of the history of the Universe, i.e. from $z \sim 2$ (or before) until today. Our evidence for this mechanism lies in the similarity in the shape of the PE galaxy SMF at $z \sim 2$ and $z \sim 0.9$, and the possibility that the $z \sim 0$ SMF contains a component that is also similar to these higher-z SMFs. The interesting question to turn to next is that of the nature of the mechanism responsible for this time-invariant, mass-dependent quenching.

ACKNOWLEDGEMENTS

We thank Taro Sato for letting us use his PSF-matched images and completeness simulations in advance of publication, and Anneya Golob, Bobby Sorba and the anonymous referee for comments that improved the quality of this manuscript. Computational facilities for this work were provided by ACEnet, the regional high performance computing consortium for universities in Atlantic Canada. ACEnet is funded by the Canada Foundation for Innovation (CFI), the Atlantic Canada Opportunities Agency (ACOA), and the provinces of Newfoundland and Labrador, Nova Scotia and New Brunswick. This research was financially supported by funds from the Natural Sciences and Engineering Research Council of Canada (NSERC) and by an ACEnet Fellowship. Parts of the analysis presented here made use of the Perl Data Language (PDL) that has been developed by K. Glazebrook, J. Brinchmann, J. Cerney, C. DeForest, D. Hunt, T. Jenness, T. Luka, R. Schwebel and C. Soeller; PDL provides a high-level numerical functionality for the PERL scripting language (Glazebrook & Economou 1997) and can be obtained from http://pdl.perl.org, while additional calculations were carried out using the online cosmological calculator of Wright (2006).

This work is based on observations obtained with MegaPrime/MegaCam and WIRCam. The former is a joint project of CFHT and CEA/DAPNIA, at the Canada–France–Hawaii Telescope (CFHT) which is operated by the National Research Council (NRC) of Canada, the Institut National des Science de lUnivers of the Centre National de la Recherche Scientifique (CNRS) of France and the University of Hawaii. The later, WIRCam, is a joint project of CFHT, Taiwan, Korea, Canada, France, at the CFHT. This work is based in part on data products produced at TERAPIX and the Canadian Astronomy Data Centre as part of the Canada–France–Hawaii Telescope Legacy Survey, a collaborative project of NRC and CNRS, and by the WIRDS (WIRcam Deep Survey) consortium. This research was supported by a grant from the Agence Nationale de la Recherche ANR-07-BLAN-0228.

REFERENCES

Baldry I. K., Glazebrook K., Driver S. P., 2008, MNRAS, 388, 945
Bell E. F., McIntosh D. H., Katz N., Weinberg M. D., 2003, ApJS, 149, 289

Bertin E., Arnouts S., 1996, A&AS, 117, 393
Bielby R. et al., 2012, A&A, 545, A23
Blanc G. A. et al., 2008, ApJ, 681, 1099
Bruzual G., Charlot S., 2003, MNRAS, 344, 1000
Calzetti D., Armus L., Bohlin R. C., Kinney A. L., Koornneef J., Storchi-Bergmann T., 2000, ApJ, 533, 682
Cimatti A. et al., 2002, A&A, 381, L68
Cowie L., Songaila A., Hu M., Cohen J., 1996, AJ, 112, 3
Daddi E. et al., 2004a, ApJ, 600, 127
Daddi E., Cimatti A., Renzini A., Fontana A., Mignoli M., Pozzetti L., Tozzi P., Zamorani G., 2004b, ApJ, 617, 746
Drory N. et al., 2009, ApJ, 707, 1595
Elsner F., Feulner G., Hopp U., 2008, A&A, 477, 503
Elston R., Rieke G., Rieke M., 1988, ApJ, 331, L77
Franx M. et al., 2003, ApJ, 587, L79
Glazebrook K., Economou F., 1997, Perl J., 5, 5
Goranova Y. et al., 2009, The CFHTLS T0006 Release
Graham A., Driver S., Petrosian V., Conselice C., Bershady M., Crawford S., Goto T., 2005, AJ, 130, 1535
Grazian A. et al., 2007, A&A, 465, 393
Gwyn S. D. J., 2012, ApJ, 143, 38
Hartley W. G. et al., 2008, MNRAS, 391, 1301
Hayashi M., Shimasaku K., Motohara K., Yoshida M., Okamura S., Kashikawa N., 2007, ApJ, 660, 72
Ilbert O. et al., 2010, ApJ, 709, 644
Kajisawa M., Ichikawa T., Yoshikawa T., Yamada T., Onodera M., Akiyama M., Tanaka I., 2011, PASJ, 63, S403
Kitzbichler M. G., White S. D. M., 2007, MNRAS, 376, 2
Kong X. et al., 2006, ApJ, 638, 72
Kron R., 1980, ApJS, 43, 305
Lane K. et al., 2007, MNRAS, 379, L25
Lilly S. J., Tresse L., Hammer F., Crampton D., Le Févre O., 1995, ApJ, 455, 108
Mancini C. et al., 2010, MNRAS, 401, 933
Marmo C., 2007, WIRCam Data Reduction at TERAPIX, v1.0
McCracken H. J. et al., 2010, ApJ, 708, 202
Merson A. I. et al., 2013, MNRAS, 429, 556
Messias H., Afonso J., Hopkins A., Mobasher B., Dominici T., Alexander D. M., 2010, ApJ, 719, 790
Oke J. B., 1974, ApJS, 236, 27
Onodera M. et al., 2010, ApJ, 715, L6
Peng Y. et al., 2010, ApJ, 721, 193
Pérez-González P. G. et al., 2008, ApJ, 675, 234
Pozzetti L. et al., 2010, A&A, 523, A13
Ravindranath S., Daddi E., Giavalisco M., Ferguson H., Dickinson M., 2008, in Bureau M., Athanassoula E., Barbuy B., eds, Proc. IAU Symp. 245, Formation and Evolution of Galaxy Bulges. Cambridge Univ. Press, Cambridge, p. 407
Reddy N., Erb D., Steidel C., Shapley A., Adelberger K., Pettini M., 2005, ApJ, 633, 748
Roche N., Almaini O., Dunlop J., Ivison R., Willott C., 2002, MNRAS, 337, 1282
Salpeter E., 1955, ApJ, 121, 161
Santini P. et al., 2009, A&A, 504, 751
Sawicki M., 2012a, PASP, 124, 1208
Sawicki M., 2012b, MNRAS, 421, 2187
Sawicki M., Thompson D., 2006, ApJ, 642, 653
Schechter P., 1976, ApJ, 203, 297
Schlegel D., Finkbeiner D., Davis M., 1998, ApJ, 500, 525
Scoville N. et al., 2007, ApJS, 172, 38
Shapley A., 2011, ARA&A, 49, 525
Steidel C., Adelberger K., Giavalisco M., Dickinson M., Pettini M., 1999, ApJ, 519, 1
Steidel C., Adelberger K., Shapley A., Pettini M., Dickinson M., Giavalisco M., 2003, ApJ, 592, 728
Steidel C. C., Shapley A., Pettini M., Adelberg K., Erb D., Reddy N., Hunt M., 2004, ApJ, 604, 534
Thompson D. et al., 1999, ApJ, 523, 100
van Dokkum P. et al., 2004, ApJ, 611, 703
Wright E. L., 2006, PASP, 118, 1711
Wuyts S., Labbé I., Föster-Schreiber N. M., Franx M., Rudnick G., Brammer G. B., van Dokkum P. G., 2008, ApJ, 682, 985
Yabe K., Ohta L., Iwata I., Sawicki M., Tamura N., Akiyama M., Aoki K., 2009, ApJ, 693, 507
Yuma S., Ohta K., Yabe K. M., Ichikawa T., 2011, ApJ, 763, 92

This paper has been typeset from a TEX/LATEX file prepared by the author.